An Attempt to Reduce Airfoil Tonal Noise Using Fluid-Structure Interaction

Di. Wu*, Garret. C. Y. Lam† and Randolph. C. K. Leung‡
The Hong Kong Polytechnic University, Hong Kong, People's Republic of China

Airfoil tonal noise at low Reynolds number has received lot of attentions due to the increasing interest in micro air vehicles. However, for decade, researchers have spent plenty of efforts to investigate the fundamental mechanism of tonal noise generation rather than its control. In the present paper an attempt to control airfoil tonal noise leveraging the fluid-structure interaction of a flexible panel installed on a NACA0012 airfoil is carried using direct aeroacoustics simulation approach. The airfoil at angle of attack of 5° is immersed in a free stream of Reynolds and Mach numbers equal 5×10^4 and 0.4, respectively. The selection of flexible panel parameters is based on the numerical results of ordinary airfoil. A modified linear stability analysis is employed to study the interaction between instability and the panel response as well as its effect on eventual tonal noise radiation. Comparison of numerical results with and without flexible panel reveals there is a great possibility of tonal noise reduction around 1.3 dB with carefully selected fluid-structure interaction.

I. Nomenclature

Re	=	Reynolds number
Ma	=	Mach number
Pr	=	Prandtl Number
c	=	sound speed
R	=	gas constant
c_p	=	specific heat at constant pressure
γ	=	ratio of specific heat
ρ	=	density
u	=	velocity along x direction
v	=	velocity along x direction
E	=	internal energy
p	=	pressure
T	=	temperature
μ	=	viscosity
q	=	heat flux
τ	=	stress
c	=	chord
V	=	volume
S	=	area
w	=	width
h	=	hight
A	=	amplitude
r	=	radiuis
L	=	length

*PhD Candidate, Department of Mechanical Engineering, The Hong Kong Polytechnic University, Hung Hom,Kowloon, Hong Kong, People's Republic of China.

†Research Fellow, Department of Mechanical Engineering, The Hong Kong Polytechnic University, Hung Hom,Kowloon, Hong Kong, People's Republic of China.

‡Associate Professor, Department of Mechanical Engineering, The Hong Kong Polytechnic University, Hung Hom,Kowloon, Hong Kong, People's Republic of China, Senior Member AIAA.

N = N-factor
$\mathrm{d}t$ = time step size
C_p = pressure coefficient
C_l = lift coefficient
C_d = drag coefficient
f = frequency

Subscript

∞ = freestream
x, y, t = x, y, t components
base = base flow
preb = perturbation
flow = flow field
fp = flexible panel
le = leading edge
te = trailing edge
far = far field

Superscript

$'$ = fluctuation
$\bar{}$ = time averaged value

II. Introduction

The research of airfoil tonal noise has received lot of attention in recent years mainly due to two considerations. First, from a fundamental standpoint, the physical mechanism of hydrodynamic stability in boundary layer and the coupled airfoil tonal noise are still not fully understand. Secondly more practical situation might be based on the wide usage of Unmanned Air Vehicles (UAV) where noise might be considered as a series nuisance.

The earliest research about the airfoil tonal noise generation might be implemented by Paterson *et al* [1] by a detail experimental based on NACA0012 and NACA0018 airfoils in a low turbulence and open-jet wind tunnel. Three different AOA cases were tested to measure the pressure fluctuations on airfoil surface and the far-field sound distributions. The results show the dominated sound frequency obeys the relationship of $f \propto \left(\sqrt{u^2+v^2}\right)^{1.5}$. Besides of the formulation to evaluate dominant frequency, the most significant finding by Paterson *et al* might be the ladder-like frequency structure that the sound frequency depends on the velocity to the 0.8 power locally. Slightly increasing in free-stream velocity usually lead to a sound frequency raising in the 'rung' of $f\left(\sqrt{u^2+v^2}\right)^{0.8}$. Paterson *et al* attributed these phenomenons to the vortex shedding process.

Tam [2] summarized Paterson *et al*'s works as following three points. Firstly, the discrete tones generated because of the existing of the laminar boundary layer on both sides of airfoil. Secondly, when the velocity of free-stream increased, the discrete tone also increased. Thirdly, the source of discrete tones is very close to the trailing edge of airfoil. However, Tam argued the opinion that the vortex shedding from the airfoil direct causes discrete tone phenomenon. Instead, a self-excited feedback loop between the trailing edge and some location in the wake is proposed to explain the discrete tone phenomenon. However, this explanation might be valid only at high Mach numbers.

Longhouse [3] proposed another explanation of airfoil tonal noise generation that the feedback loop happens between the trailing edge and an location in upstream on the airfoil surface. Usually, that location is regarded as the place that instability behaviour begins. Subsequent research by Arbey *et al* [4] further improved Longhouse's hypothesis that they believe the location that the instability behaviour begins should be the maximum velocity point. Furthermore, Arbey *et al* also shown that if instability wave and acoustic wave have same phase at maximum velocity point, the ladder like frequency structure will arise.

Brooks *et al* [5] gave a good summery about the prediction method of airfoil self-noise problem. Although seldom of physical mechanism are touched, the calculation processes to predict the turbulent boundary layer – trailing edge noise, laminar boundary layer – vortex shedding noise and tip vortex formation noise are well reviewed.

With the development of the equipments, new experiments were carried out on a NACA0012 aerofoil in a low-turbulence closed wind tunnel by Nash *et al* [6]. Different with previous researchers results, only a single dominant tonal frequency without any ladder-like structure is found. Nash *et al* attribute these phenomenons to a more carefully controlled experimental environment. Followed, a new tonal noise generation mechanism based on the vortex-shedding produced by the instability waves is proposed. Different with the explanations given by previous researchers, Nash *et al* believed the feedback loop was not a necessary condition for the generation of tonal noise. In particular, the massively amplified instability wave causes vortex shedding happens. Then the interaction between the vortex and trailing edge leads to a noise generation. During this process, the most amplified frequency of instability wave is identical to the sound dominated frequency.

Extensive numerical investigation is given by Desquesnes *et al* [7] to support the idea that there is a deep relationship between the dominant sound frequency and the most amplified instability wave frequency. Moreover, authors also proposed that the phase difference of instability wave on both suction and pressure side might be a key point to affect the tone noise generation. Which implies there might be a cross-talk between the suction and pressure side. This idea is also supported by de Pando*et al* [8]. Later Jones *et al* [9, 10] conducted a numerical investigation to further support the Nesh *et al* and Desquesnes *et al*'s work that the tonal noise is caused by the vortices rolling over the airfoil trailing edge. Besides of that, the feedback looping is also simulated successfully by applying N-S equation with source term.

Even the fundamental mechanism of tonal noise generation has been widely studied, the use of knowledge for a noise reduction is still rare. Many researchers seem prefer a treatment on trailing edge [11–14], such as sawtooth trailing edge, rather than suppressing the instability wave amplification, to decrease the noise generation. The present study aims to explore the possibility of airfoil tonal noise reduction by modifying the instability wave development with fluid-structure interaction imposed by a flexible panel on airfoil surface.

The paper is organized as follows. The research methodology will be introduced in Section III. Followed, a validation by comparing the solutions of current study and previous researchers works will be given in Section IV. Based on the solution obtained from Section IV, a two-dimensional modified linear stability analysis is implemented in Section V. This is aimed at giving a more solid foundation for the further stability analysis on airfoil with flexible panel. Followed, a linear stability analysis results based on the airfoil with and without flexible panel is also presented.

III. Research Methodology

In the present study, we apply direct aeroacoustic simulation approach [15, 16] for its inherent capability of resolving the interaction between the flow dynamics and acoustics which is essential in studying the aeroacoustic phenomenon involving possible feedback mechanism. A brief introduction of the governing equations of DAS will be presented. Since there are works highlight the important role of the amplification instability wave process on airfoil suction surface in trailing edge tonal noise generation, the two-dimensional linear stability theory (LST) will be attempted in presented study because it effectively provides qualitative and quantitative hydrodynamic stability responses of in shear flows, the results of which may shed light on the connection between instability wave processes and tonal noise characteristics. However, it should be pointed out that, LST requires a time averaged base flow which are obtained from prior DAS calculations with sufficiently high resolution.

A. Direct Acoustic Simulation

The governing equations of DAS of a two dimensional flow past an airfoil, namely compressible Navier-Stokes (N-S) equations and the equation of state, are solved simultaneously. The N-S equations can be written in strong conservative form as

$$\frac{\partial \boldsymbol{U}}{\partial t} + \frac{\partial (\boldsymbol{F} - \boldsymbol{F_v})}{\partial x} + \frac{\partial (\boldsymbol{G} - \boldsymbol{G_v})}{\partial y} = 0 \tag{1}$$

which are normalized by reference density, ρ_∞, velocity, V_∞, viscosity, μ_∞, temperature, T_∞, and specific heat at constant pressure, $c_{p\infty}$ in free stream flow and the reference chord length. The reference sound speed is defined as $c_\infty = \sqrt{\gamma R T_\infty}$, where γ=1.4 is the ratio of specific heat and the gas constant, R=287.058 J/(kg K) of air. Therefore, the Re, and Ma can be calculated as

$$Re = \frac{\rho_\infty V_\infty \mathrm{c}}{\mu_\infty}, Ma = \frac{V_\infty}{c_\infty}, Pr = \frac{\mu_\infty c_{p\infty}}{k_\infty} = 0.72 \tag{2}$$

where k_∞ is reference thermal conductivity. In Eq. (1), the definition of $\boldsymbol{U}$, $\boldsymbol{F}$ and $\boldsymbol{G}$ are given by

$$\boldsymbol{U} = \begin{bmatrix} \rho \\ \rho u \\ \rho v \\ \rho E \end{bmatrix}, \boldsymbol{F} = \begin{bmatrix} \rho u \\ \rho u^2 + p \\ \rho uv \\ (\rho E + p)\, u \end{bmatrix}, \boldsymbol{G} = \begin{bmatrix} \rho v \\ \rho uv \\ \rho v^2 + p \\ (\rho E + p)\, v \end{bmatrix} \tag{3}$$

where E and p are the internal energy and pressure defined as

$$E = \frac{p}{(\gamma - 1)\,\rho} - \frac{\left(u^2 + v^2\right)}{2} \tag{4}$$

and

$$p = \frac{\rho T}{\gamma M a^2} \tag{5}$$

The viscous flux vectors $\boldsymbol{F_v}$ and $\boldsymbol{G_v}$ are defined as

$$\boldsymbol{F_v} = \frac{1}{Re}\begin{bmatrix} 0 \\ \tau_{xx} \\ \tau_{xy} \\ \tau_{xx}u + \tau_{xy}v - q_x \end{bmatrix}, \boldsymbol{G_v} = \frac{1}{Re}\begin{bmatrix} 0 \\ \tau_{xy} \\ \tau_{yy} \\ \tau_{xy}u + \tau_{yy}v - q_y \end{bmatrix} \tag{6}$$

where τ_{xx}, τ_{xy} and τ_{yy} are stress terms such that

$$\tau_{xx} = \left(\frac{4}{3}\frac{\partial u}{\partial x} - \frac{2}{3}\frac{\partial v}{\partial y}\right)\mu, \tau_{xy} = \left(\frac{\partial u}{\partial x} + \frac{\partial v}{\partial y}\right)\mu, \tau_{yy} = \left(\frac{4}{3}\frac{\partial v}{\partial y} - \frac{2}{3}\frac{\partial u}{\partial x}\right)\mu \tag{7}$$

and the thermal fluxes are

$$q_x = -\frac{1}{Pr}\frac{\mu}{(\gamma - 1)\,Ma^2}\frac{\partial T}{\partial x}, q_y = -\frac{1}{Pr}\frac{\mu}{(\gamma - 1)\,Ma^2}\frac{\partial T}{\partial y} \tag{8}$$

B. Modified Linear Stability Analysis

In essence, LTS act to decompose any incompressible flow quantity, $\boldsymbol{q}$, into a local steady base flow and an unsteady infinitesimally weak perturbation as [17–19],

$$\boldsymbol{q} = \boldsymbol{q}_{base} + \boldsymbol{q}_{preb} \tag{9}$$

The perturbation may be further expressed as a superposition of Fourier modes wiht i-th, one given by

$$\boldsymbol{q}_{preb,i}\,(x, y, t) = \hat{\boldsymbol{q}}_{\boldsymbol{i}}\,(y)\, e^{i(\alpha x - \omega t)} \tag{10}$$

where $\hat{q}_i$ is the complex amplitude of the perturbation. The variable α is the complex wavenumber and ω is the complex frequency.

Traditionally, the base flow is assumed to satisfy

$$\boldsymbol{U}_{base} = (u_{base}, v_{base}) \approx (u\,(y), 0), \quad p_{base} = p\,(y) \tag{11}$$

Substituting Eq. (9) into two-dimensional incompressible Navier-Stokes (N-S) equations and ignoring the terms quadratic in perturbation velocity, coupled with Eqs.(10) and (11), the well-known Orr–Sommerfeld (O-S) equation result [19].

$$\left(u_{base} - \frac{\omega}{\alpha}\right)\left(\frac{d^2\hat{v}}{dy^2} - \alpha^2\hat{v}\right) - \frac{d^2 u_{base}}{dy^2}\hat{v} = -\frac{i\nu}{\alpha}\left(\alpha^4\hat{v} - 2\alpha^2\frac{d^2\hat{v}}{dy^2} + \frac{d^4\hat{v}}{dy^4}\right) \tag{12}$$

If the base flow is specified, then the O-S equation can be converted to a linearized eigenvalue problem in the form $\boldsymbol{A}\hat{v} = \boldsymbol{B}\hat{v}$, where $\hat{v}$ is the eigenvector. The mathematical framework of this apporch has been reviewed and discussed in many existing literatures. [17–20].

Linear stability analysis with O-S equation have been widely used in many studies of boundary layer over flat plate for a long time. The assumption of quasi-parallel base flow prompts to adopt the steady laminar boundary layer solution in the studies [2, 4] and the Hartee profiles to cater for the effects of adverse pressure gradient [6, 21]. However, these

treatments are not suitable for the analysis of the boundary layer on the curved airfoil suction surface. Therefore, a modified linear stability analysis (MLSA) method of solving the evolution of infinitesimal perturbation in boundary layer using N-S equations with source term is adopted [10, 22]. The governing equation may thus be written as

$$\cdot\frac{\partial \boldsymbol{U}}{\partial t}+\frac{\partial \boldsymbol{F}}{\partial x}+\frac{\partial \boldsymbol{G}}{\partial y}=\left(\frac{\partial \boldsymbol{F}}{\partial x}+\frac{\partial \boldsymbol{G}}{\partial y}\right)_{base} \tag{13}$$

Since the base flow is steady,

$$,\frac{\partial \boldsymbol{U}_{base}}{\partial t}=0 \tag{14}$$

and similar to Eq.(**??**),

$$\cdot\frac{\partial \boldsymbol{F}}{\partial x}+\frac{\partial \boldsymbol{G}}{\partial y}=\left(\frac{\partial \boldsymbol{F}}{\partial x}+\frac{\partial \boldsymbol{G}}{\partial y}\right)_{base}+\left(\frac{\partial \boldsymbol{F}}{\partial x}+\frac{\partial \boldsymbol{G}}{\partial y}\right)_{perb} \tag{15}$$

If the initial condition is just the steady base flow, substituting Eq. (9) and (15) into Eq. (13), gets

$$,\frac{\partial\left(\boldsymbol{U}_{base}+\boldsymbol{U}_{preb}\right)}{\partial t}+\left(\frac{\partial \boldsymbol{F}}{\partial x}+\frac{\partial \boldsymbol{G}}{\partial y}\right)_{perb}=0 \tag{16}$$

which may be further written as follows with the use of Eq. (14)

$$\cdot\frac{\partial \boldsymbol{U}_{preb}}{\partial t}+\left(\frac{\partial \boldsymbol{F}}{\partial x}+\frac{\partial \boldsymbol{G}}{\partial y}\right)_{perb}=0 \tag{17}$$

Comparing to the stability analysis of solving O-S equation, the Eq. (17) has less limitations.

For the sake of simplicity the base flow is commonly taken from the velocity profiles calculated from steady boundary layer equation. Now, with the availability of high performance computer, researchers prefer to take the time averaged flow field of the problem as the base flow for its more faithful description [7, 8, 22]. Therefore the same approach is adopted in the present study.

Besides the perturbation that is used to initiate the flow instability evolution requires some care. In the work of Jones *et al* [22], a continuously periodic volume forcing is applied within the boundary layer. On the other hand, de Pando*et al* suggests an artificial pulse used as the external excitation. In essence an artificial weak pulse is initiated at an upstream location very close to the airfoil which will be conveyed by the evolution of the N-S solution to hit the airfoil leading edge and cause the actual perturbation required for the stability analysis. The same approach is adopted and artificial pulse is defined by a Gaussian function,

$$\begin{gathered}
p\left(x,y\right)=0 \\
\rho_{base}\left(x,y\right)u\left(x,y\right)=-A\frac{\left(y-y_p\right)}{r}\exp\left(-\frac{\left(x-x_p\right)^2+\left(y-y_p\right)^2}{r^2}\right) \\
\rho_{base}\left(x,y\right)v\left(x,y\right)=A\frac{\left(x-x_p\right)}{r}\exp\left(-\frac{\left(x-x_p\right)^2+\left(y-y_p\right)^2}{r^2}\right)
\end{gathered} \tag{18}$$

where A and r are the pulse amplitude and radius, respectively. Moreover, the pulse central location is decided by both x_p and y_p.

C. Solution Method

The DAS is solved numerically with Conversation Element and Solution Element (CE/SE) method in presented study. The CE/SE method is a high resolution and genuinely multidimensional method for solving conservation laws. It has been used to obtain high accurate numerical solutions for aeroacoustics problem at low Mach number [15, 16].

In order to apply CE/SE method in MLSA, some modifications are needed. We modified Eq.13 as

$$,\frac{\partial \boldsymbol{U}}{\partial t}+\left(\frac{\partial \boldsymbol{F}}{\partial x}-\left(\frac{\partial \boldsymbol{F}}{\partial x}\right)_{base}\right)+\left(\frac{\partial \boldsymbol{G}}{\partial y}-\left(\frac{\partial \boldsymbol{G}}{\partial x}\right)_{base}\right)=0 \tag{19}$$

Mesh size					
$w_{le} \times 10^4$	$h_{le} \times 10^4$	$w_{te} \times 10^4$	$h_{te} \times 10^4$	$w_{far} \times 10^2$	$h_{far} \times 10^2$
5	6	9	6	1	1

Table 1 Mesh size with different locations

which can be Integrated as,

$$\iint \frac{\partial \boldsymbol{U}}{\partial t} dV + \iint \left(\frac{\partial \boldsymbol{F}}{\partial x} - \left(\frac{\partial \boldsymbol{F}}{\partial x} \right)_{base} \right) dV + \iint \left(\frac{\partial \boldsymbol{G}}{\partial y} - \left(\frac{\partial \boldsymbol{G}}{\partial x} \right)_{base} \right) dV = 0 \tag{20}$$

where V is the volume of CE. Applying Gauss' law to Eq.20, we get

$$\int_{CE} (\boldsymbol{U})\, d\overrightarrow{s_t} + \int_{CE} (\boldsymbol{F} - \boldsymbol{F}_{base})\, d\overrightarrow{s_x} + \int_{CE} (\boldsymbol{G} - \boldsymbol{G}_{base})\, d\overrightarrow{s_y} = 0 \tag{21}$$

where $\overrightarrow{s_t}$, $\overrightarrow{s_x}$ and $\overrightarrow{s_y}$ are unit normal vector along t, x and y axes in three-dimensional Euclidean space. The second and third terms in the left hand of Eq.21 can be decomposed as,

$$\begin{aligned} \boldsymbol{F}_{preb} &= \boldsymbol{F} - \boldsymbol{F}_{base} \\ \boldsymbol{G}_{preb} &= \boldsymbol{G} - \boldsymbol{G}_{base} \end{aligned} \tag{22}$$

Then substituting Eq.22 into Eq.21, gives

$$\int_{CE} \boldsymbol{U} d\overrightarrow{s_t} + \int_{CE} \boldsymbol{F}_{preb} d\overrightarrow{s_x} + \int_{CE} \boldsymbol{G}_{preb} d\overrightarrow{s_y} = 0 \tag{23}$$

which restores to the original form of equation to solve the CE/SE method but with different variables.

D. Numerical Settings

The airfoil adopted takes a NACA0012 profile. The flow parameters are selected as $Re = 5 \times 10^4$, $Ma = 0.4$ and an angle of attack of 5°. These parameters are also identical to the work of Jones *et al.* work [9]. so that, a rigorous comparison is possible.

A Cartesian coordinate is with he original set at the airfoil leading edge. The airfoil trailing edge is located at $(x,\ y) = (1,\ 0)$. The physical domain is a rectangle region with a length of 6.0 and height of 6.5. In order to eliminate the error numerical wave from domain boundary, a buffer zone with a offset of 1.5 is set surrounding the physical domain. Although Jones *et al* [9] suggested that a rectangle region for wake development should be made long enough to ensure that the vortices can fully develop, subsequent calculation will show that a narrow domain width of 3.5 is also found satisfied the requirement of accuracy. An overview of calculation domain in shown in Fig.1.

The mesh size around airfoil leading edge, trailing edge and in far field are given special attentions because they will affect the accuracy of boundary layer evolution and noise propagation significantly. The mesh sizes with different locations are listed in Tab.1 and illustrated in Fig.1(b-d). The total amount of quadrangle meshes used is 1.63×10^6. In order to get a high resolution result, a diagonal cross division is used to split one quadrangle mesh into four triangle meshes. Therefore, the total amount of meshes in calculation is four times of quadrangle mesh amount. Based on the mesh size, the time step size, d$t = 1 \times 10^{-5}$ is set for all calculations

The non-reflect boundary condition is applied on the boundaries of buffer to further eliminate any numerical wave reflection. On the airfoil surface, the no-slip boundary condition is applied.

IV. Verification of DAS Results

A. Flow dynamics

Time averaged flow field

Fig.2 shows the distribution of calculated pressure coefficient c_p. In order to make the comparison, the solutions by Jones *et al* is also plotted. On the suction side, the CE/SE result shows a rapidly increase near the leading edge of $0.04<x<0.2$; this implies a strongly adverse pressure gradient exists which slow down the flow. A pressure plateau can be found in $0.2<x<0.45$, followed by a rapid increase in $0.44<x<0.6$. When $x>0.6$, the c_p keeps in a small negative value and shows a very slight growth rate. Comparing to the Jones *et al* solution, an offset about 3% can be observed in $0.02<x<0.4$, which implies the solution by CE/SE is in agreement with the Jones *et al* solution. In the region of $0.4<x<0.6$, better agreement prevails. It can be seen that a rapid increase happens around x=0.5 in both case, which further implies the high accuracy of CE/SE solution agrees well with the FDM one.

From the C_f distribution in Fig.3, the separation point and reattachment point can be found where C_f crosses the zero. It is apparent that the separation occurs at $x_{se} = 0.18$ and reattached at $x_{re} = 0.58$. Comparing to the Jones *et al* results of $x_{se} = 0.144$ and $x_{re} = 0.582$, a good agreement can be found in the position of reattachment point. However, a slight divergence can be found in the comparison of separation point.

Unsteady flow field

A comparison of flow fields obtained from CE/SE solution and Jones et al. is given in Fig.4. Nearly identical flow fields are resulted. It can observed that the vortex shedding mainly happens around x=0.6, which is consistent to the C_f that the separation bubble growth ending at x=0.58.

Fig.5 shows a comparison of C_l and C_d from CE/SE to existing results in literature. It is observed that the C_l and C_d by CE/SE solutions oscillate periodically with a range of $0.47<C_l<0.52$ and $0.0197<C_d<0.0255$, respectively, which are in good agreement with the results by Jones *et al* [9] and filtered N-S equation result by Almutairi *et al*. [23]. The time averaged C_l and C_d can be calculated based on the time histories. The time averaged C_l and C_d by CE/SE is 0.4947 and 0.0229, respectively. Comparing to corresponding values of 0.4990 by Jones *et al* and 0.4950 by Almutairi *et al*, the maximum divergence is only 0.86%. Furthermore, the presented time averaged C_d differs from the Jones *et al* result of 0.022 by 3.6% only, which clearly shows the high accuracy of CE/SE solution.

The fast Fourier transform (FFT) results are shown in Fig.6. In order to obtain a high resolution result, a full length time history which contains 10 calculation time with an sample frequency of 1×10^5 is used. The FFT results show the first dominant frequencies of C_l and C_d happen at 3.37 and 3.3, respectively. The slight frequency deviation between C_l and C_d might be due to the effect of frictional drag. Comparing corrseponding frequencies of C_l of 3.371 in Ref.[9] and of 3.375 in Ref.[23], a good agreement can also be found. Besides, the second and third dominant frequencies are found in CE/SE solution. This multiple frequency characteristic in the hydrodynamic fluctuation should receive more considerations when selecting the flexible panel parameters.

B. Noise radiation

The time averaged acoustics pressure distribution at radius two chords are plotted by p_{TA}/p_∞ in Fig.7 and compared with the FDM solution. It is apparent that the solution by CE/SE are in a good agreement with the FDM solution. The maximum difference is only 0.2% which happens at $\theta \approx 120^\circ$. A typical pressure fluctuation map is plotted in Fig.8(a) and compared with the FDM solution. Notice that Fig.8(b) is presented by $\nabla \boldsymbol{U}$. It can be seen that the acoustic waves are continuously generated from wake near the trailing edge and radiate to entire flow field. However, it should be pointed out that the acoustic waves do not distribute uniformly in all directions. It is apparent that most of them are spreading towards the forward half-plane. For the suction side, the acoustic waves show an angle of 40° with the chordwise towards the upstream. And for the pressure side, the angle is decreased to 30°. This divergence might be due to the angle of attack in current study is not zero. Further FFT analysis shows the first dominated frequency of acoustic field is 3.371, which coincides with Jones *et al*'s and Jaber *et al*'s solutions.

A rigorous verification process is implemented in this suction. The calculation results shows both the flow field and acoustic field agree well with the previous researchers' works, which strongly suggests our calculation is reliable. Based on the solutions of DAS, the time averaged flow will be calculated and applied as base flow in LST process in next section.

V. Results and Discussion

In this section, the calculation results from MLSA will be presented. Firstly, a base case is calculated and compared with the solutions by solving O-S equation and three-dimensional result of Jones *et al*. This process can be regarded as a verification of our LST code. Followed, the MLSA results on airfoil with flexible panel will be presented and compared with the ordinary airfoil.

A. A Base Case

Fig.9 shows the v component fluctuation, denoted as v' from t=0.0 to 0.2. The initial condition is presented in Fig.9(a). It can be seen that the artificial pulse is initialized very closed to the airfoil leading edge. When the pulse parameters, some key points need to be considered. Firstly, the pulse amplitude should be small enough to meet the assumption of infinitesimal perturbation. Otherwise, the perturbation development might goes in to a non-linear region and causes the LST invalid. Secondly, the pulse should not be too far away from the airfoil in case it has decayed to zero before hitting the leading or trailing edge. Therefore, in current calculation, the amplitude and radius are set as $A = 0.0001$ and $r = 0.005$, respectively. Moreover, the pulse location is given as $x_p = -0.015$ and $y_p = -0.01$.

Due to the transport effect of flow, the pulse hits against the leading edge with the time marching of calculation. Fig.9(b) shows the v' variation snapshot when the impact happens. An acoustic wave packet generates due to the impact and spreads into entire flow field. This phenomenon is also observed by de *et al* [8]. Moreover, the impact leads to a perturbations injection into the boundary layers on both airfoil suction and pressure sides. These perturbations are treated as the initial infinitesimal perturbations in linear stability theory and will be investigated in following work. When time goes to $t = 0.1$, it can be seen that the initial perturbations turn to a downstream-travelling instability wave. The structure of instability wave might be described as alternately positive and negative v' regions. More clearly structure can be observed in Fig.9(d) and (e). It is worth noting that similar structure denoted as mutil-lobed structure are also found by Jones *et al* [22] presented by the dilatation of flow field quantities fluctuation. Moreover, it should be pointed out that, even both suction and pressure side boundary layers are disturbed, the downstream-travelling instability wave is only found on the airfoil suction side. This might because a strong positive pressure gradient is existed on airfoil pressure side, which will lead a fast decay of instability wave. A similar observation is also found in de Pando *et al*'s work [8].

The subsequent flow field evolution is presented in Fig.10. For $0.3 \leqslant t \leqslant 0.7$, the instability wave is continuously travelling towards the trailing edge. At the same time, a gradual amplification of the instability wave can be observed. Fig.10 shows this amplification mainly happens when the instability wave is travelling in separation bubble from $0.15 < x < 0.58$. This observation is in agreement with the previous linear stability analysis results of solving the O-S equation that the boundary layer convectively unstable mode caused by adverse pressure gradient leads to a strongly spatial growth of instability wave [4, 6]. For the pressure side, a clean flow filed is observed, which further implies the initial perturbations is fully damped in the early stage of impact. Although some researchers suggested the separation on pressure side will also lead a similar instability wave amplification or a cross-talk mechanism between suction and pressure sides [8, 24], in current investigation, a 5 degree angle of attack ensures there is no separation happens on pressure side. Therefore, no more detail discussion about the instability wave behaviour on pressure side will be presented.

During the computational time $1.1 \leq t \leq 1.7$, Fig.11 represents the flow field variation. It can be seen clearly that the downstream-travelling instability wave reaches the trailing edge at $t \approx 1.3$. After passing the trailing edge, the instability wave produces upstream-travelling waves in both upper and lower half-planes. The spreading speed of upstream-travelling wave might be estimated by Fig.11(c) and (d). The calculation results shows the spreading speed of upstream-travelling wave is around 1.5 which is in agreement with the sound speed if taking the Doppler effect into consideration. Therefore, the upstream-travelling waves can be regarded as acoustic wave.

In order to give a quantitative view of instability wave amplification process, the time histories of flow quantities will be used. However, before the analysis, a validation is needed to ensure the infinitesimal assumption is kept in current calculation, otherwise the calculation might goes into the nonlinear region and the linear stability theory will be invalid. Because previous studies has shown that the instability wave amplification mainly happens in separation bubble, therefore, the flow quantities fluctuation at the location after the reattachment point should be given more attentions. The v' time histories of $0 \leq t \leq 4$ at four locations of $x = 0.7$, 0.8, 0.9 and 1.0 are shown in Fig.12. It can be observed that the v' time histories mainly oscillate in a range of $\pm 1\%$ times the free stream velocity during $0 \leq t \leq 4$. This might be small enough to regards that the development of instability wave is still in linear region. A similar threshold of $\pm 1\%$ is also chosen by Tam *et al* in a non-parallel linear stability analysis to investigate the energy source in aerofoil tonal noise generation [24]. Therefore, it is safe to believe that the perturbation is still in linear region up to $t = 4$.

In order to give a insightful view of the instability wave amplification, the wave amplitude function might be calculated. Since the instability wave grows spatially along the chordwise, the wave amplitude can be regarded as a function depended on the chordwise location.

$$A(x) = A_0(x_0) \exp(N(x)) \tag{24}$$

where $A_0(x_0)$ is the initial instability wave amplitude at the reference location x_0 and $N(x)$, called by N-factor, is defined

as the spatial growth ratio of instability wave amplitude. However, it can be seen in Eq. (24) that the wave amplitude, $A(x)$, is not only depended on the N-factor but also the reference location x_0 or initial instability wave amplitude $A_0(x_0)$. Therefore, the value of $A(x)$ might be different even between two identical calculations if the reference locations or initial wave amplitudes are different. In order to overcome this limitation, a comparison between N-factor rather than $A(x)$ might be more effective. Based on the Eq. (24), the N-factor can be calculated as

$$N(x) = ln\frac{A(x)}{A_0(x_0)} \tag{25}$$

Thus, it can be observed from Eq. (25) that the N-factor only depends on the chordwise location.

In current study, the initial disturbance amplitude A_0 is selected as the disturbance amplitude at location $x = 0.05$, then the N-factor can be calculated by applying FFT to the v' time history on each virtual probe. In practical, because we focus on the amplification process of instability wave, therefore, only a short episode of time history that contains the entire instability wave will be used. The v' time histories at ten typical locations of $x = 0.05$ to 0.5 with interval 0.05 are presented in Fig.13 and Fig.14. The time episode to apply FFT is highlighted by light red region. It can be observed that both the amplitude and wavelength of the instability wave are changing along the chordwise. Then, the N-factor at each frequency can be calculated. In current study, the N-factor at three different frequencies of 4.24, 8.49 and 12.37 are calculated and compared with Jones *et al*'s works [22]. The results are shown in Fig.15. A consistent tendency can be observed that the N-factor calculated by solving two-dimensional O-S equation has the largest value for all three frequencies, followed by the three-dimensional and two-dimensional N-S equations solutions. The divergence between the solutions of O-S and N-S equations might be due to the assumption of quasi parallel flow. Between the two solutions by N-S equations. it can be seen that the three-dimensional one always grows faster than the two-dimensional one. This is in agreement with the previous numerical simulation results that the transition happens earlier in three-dimensional calculation than two-dimensional one, which implies the instability wave grows more rapidly in three-dimensional boundary layer [22]. Besides of the comparison with previous researcher' works, it can be also observed that the amplification mainly happens in $0.2 \leq x \leq 0.45$ for all three frequencies. After $x = 0.45$, the tendency of $N - factor$ became divergent. For low frequency, such as $f = 4.24$, a remarkably powerful growth rate is kept. However, for medium frequency, such as $f = 8.49$, the $N - factor$ shows a slower growth rate. And for even higher frequency, such as $f = 12.37$, the $N - factor$ became decreasing. The divergence of $N - factor$ strongly implies the instability wave with low or medium frequency should be given more attentions. Moreover, a consistent result with previous researchers works strongly implies our stability analysis process is reliable, which will give a good basics to make the analysis of airfoil with flexible panel.

B. Parameters selection of flexible panel

In current, only one membrane type flexible panel is concerned because the purpose of this paper is aimed to a fundamental mechanism study of interaction between flexible panel vibration and flow field responds. Among all of flexible panel parameters, the location of flexible panel might be the most important one because it will greatly affect not only the noise generation, but also the performance of airfoil aerodynamics. Therefore, the selection of panel location becomes the first parameter to discuss. In order to better analysis the flow fluctuation, the flow quantities of v' calculated in Section IV is used. Fig.16 shows the v' variation of the first and second dominated frequencies, denoted as $f_{flow,1}$ and $f_{flow,2}$, along chordwise. It can be observed that both the amplitude of two dominated frequencies begin to increase after $x = 0.27$. Especially in $0.4 \leqslant x \leqslant 0.45$, a remarkable growth is observed. However, when $x \geqslant 0.45$, some divergences can be found. For the first dominated frequency, it reaches a the maximum growth rate of amplitude in $0.45 \leqslant x \leqslant 0.5$. Then a high level plateau is observed in $0.5 \leqslant x \leqslant 0.57$. After that, a rapid decreasing happens. For the second dominated frequency, contrary to a remarkable growth rate of first dominated frequency amplitude, a noticeable low level trough can be found in $0.45 \leqslant x \leqslant 0.5$. Then the amplitude of second dominated frequency begins to increase and reaches a peak at $x \approx 0.57$. After that, a rapid decreasing can be observed, which is similar to the tendency of first dominated frequency. It is worth noting that both of the amplitudes of $f_{flow,1}$ and $f_{flow,2}$ mainly increase in a range of $0.27 \leqslant x \leqslant 0.57$ which is coincident with separation bubble. Moreover, the linear stability analysis by current study and previous stability analysis of solving O-S equation also shown that the existing of separation bubble lead to a drastic amplification of instability wave. Therefore, applying flexible panel in the separation bubble to suppress the rapidly growth rate of flow fluctuation might be a reasonable choice. Since both two dominated frequencies has a remarkably amplification in $0.4 \leqslant x \leqslant 0.45$, with the purpose of suppressing the amplification of both two dominated frequencies in an early stage, the leading edge of flexible panel is set at $x = 0.4$ in current study.

Besides of the location, the size of flexible panel, denoted as L_{fp}, is another important parameter. The selection

Flexible panel parameters								
Geometry parameters			Materials parameters			Natural frequency		
x	L_{fp}	h_{fp}	T_{fp}	ρ_{fp}	Damping	$f_{fp,1}$	$f_{fp,2}$	$f_{fp,3}$
0.40	0.05	0.009	4.023	6367.347	0	0.7763	1.9705	3.3123

Table 2 Flexible panel parameters

of panel size has two concerns in current study. Firstly, since the flexible panel is used to substitute part of airfoil surface, this implement implies one assumption that the ratio between panel size and local curvature radius should be infinitesimal. Otherwise this part of airfoil surface cannot be approximated as a flat panel. Therefore, for the first concern, the size of flexible panel should be small enough. However, for the second concern, a conflicting requirement might be found. If the panel size is too small, the effect of flexible panel given to the flow filed might also be limited, which will further weaken the noise reduction. Therefore, for the second concern, the size of flexible panel cannot be too small. Based on these two concerns, the panel size is chosen as $L_{fp} = 0.05$ in current study. The ratio between panel size and local curvature radius less than 1.5%, which might be small enough to treat part of airfoil surface as a flat panel. The curvature radius can be calculated by

$$r(x) = \frac{\left(1 + \left(\frac{dy}{dx}\right)^2\right)^{\frac{3}{2}}}{\left|\frac{d^2y}{dx^2}\right|} \tag{26}$$

where $y = y(x)$ is the function of NACA0012 geometry.

For the other parameters of flexible panel, such as density, ρ_{fp}, thickness, h_{fp}, internal tension, T_{fp}, and mode number, N_{fp}, they may be determined when selecting the natural frequency f_{fp}. Since the first dominated frequency of flow field is $f_{flow,1} = 3.3$, therefore, in order to lead a resonance happens, the flexible panel should has an identical natural frequency. However, it is worth noting that the natural frequency of flexible panel calculated in vacuum is not accurate enough because the external hydrodynamic force is existing in current study. For the calculation of natural frequency vibrating in flow field, Eq. (29) might be used [25]

$$f_{fp} = \left(1 + \frac{\rho_f}{N_{fp} h_{fp} \rho_{fp}}\right)^{-0.5} \left(\frac{T_{fp}}{\rho_{fp} h_{fp}}\right)^{0.5} / \left(\frac{L_{fp}}{N_{fp}^2}\right) \tag{27}$$

It should be pointed out that Eq. (29) does not take the flow velocity into consideration. Therefore, the natural frequencies calculated by Eq. (29) still cannot be identical to the counterparts by full simulation. However, it is much more accurate than the calculation in vacuum. In order to make the natural frequency equal to the first dominated frequency of flow fluctuation, the density, thickness and internal tension are chosen. Tab.2 summarizes the parameters selection. It can be observer that the third flexible panel natural frequency, denoted as $f_{fp,3}$, is 3.3123, which is almost same as $f_{flow,1}$.

Moreover, notice the calculation code of flexible panel in current study has been validated by Fan *et al.* [26–28].

C. MLSA results of airfoil with flexible panel

Based on the brief consideration, the MLSA calculation on airfoil with flexible panel is denoted as FP case. On the other hand, the calculation on rigid surface airfoil is denoted as RS case. Fig.17 shows the v' variation of FP case in $0 \leqslant t \leqslant 1$. The initial condition of simulation can be found in Fig.17(a) that the artificial pulse is initialized at $(x, y) = (0.35, 0.07)$. With the running of calculation, the artificial pulse impacts the suction side which causes an wave packet generation and spreads to entire flow filed. The propagation speed of wave packet can be estimated by Fig.17(a) and (b). It is found that the propagation speed is in agreement with the sound speed when taking the Doppler effect into consideration. Therefore, this wave packet can be regarded as an acoustic wave. A similar observation also happens when the artificial pulse is hitting against the leading edge in Section V. Besides of the wave packet generation, the instability wave is also found on the suction side. The structure of instability wave might be described as an alternately positive and negative v' region, which is also identical with the Jones *et al*'s work. After $t = 0.4$, Fig.17(c) and (d) show

x	v'_{rms}		
	FP	RS	Difference (%)
0.8	1.0648×10^{-3}	1.3008×10^{-3}	-18.1427
0.9	1.7855×10^{-3}	2.1038×10^{-3}	-15.1300
0.99	3.3822×10^{-3}	3.9487×10^{-3}	-14.3465

Table 3 v'_{rms} comparison between FP case and RS case with altered locations.

an amplification of instability wave travelling on airfoil suction side. Finally, when the instability wave reaches the trailing edge, an acoustic scatter can be observed.

In order to give a better investigation of the effect of flexible panel, the instability wave closed to trailing edge might be a good start point to analysis because the acoustic scatter is mainly caused by the instability wave passing the trailing edge. Therefore, if the instability wave around trailing edge is weakened by the flexible panel, then there might be a great possibility to lead a noise reduction. Based on the consideration above, the v' time histories at locations x =0.8, 0.9 and 0.99 is plotted in Fig.18. Notice that the calculation of airfoil with flexible panel is denoted as FP case. On the other hand, the rigid surface airfoil is denoted as RS case. It can be observed that the instability wave is amplified along the chordwise in both FP and RS cases. This observation is in agreement with the stability analysis results in Section V, which further suggests the application of flexible panel does not break the amplification of instability wave. Moreover, comparing the solutions of FP case and RS case, it can be found that a reduction of v' magnitude happens. Therefore, it might regards that the instability wave is weakened by the flexible panel.

In order to give a quantitative view of instability wave reduction, the *rms* value of v', denoted as v'_{rms}, is calculated. However, it should be noted that in current *rms* calculation, only a part of v' time histories which contains five full periods is used. The time episode used to calculate *rms* value is highlighted by light blue region in Fig.18. It is also worth noting that the maximum magnitude of v' in this time episode is around ±1% times the free stream velocity. Therefore it can be regarded that the development of instability wave is still in a linear region. The calculation results are shown in Tab.3 Notice that the negative value in "difference" column means a reduction happens, which is calculated by

$$Difference = \left(\frac{v'_{rms,FP}}{v'_{rms,RS}} - 1 \right) \times 100\% \tag{28}$$

From Tab.3, it is found that the v'_{rms} for all three locations are decreased. The maximum decreasing of 18.1427% happens at x=0.8. When the instability wave reaches the trailing edge, the v'_{rms} still shows a decreasing of 14.3465%. This strongly suggests the instability wave has been weakened by the flexible panel. Furthermore, it also implies there will be a noise reduction in far field.

For the noise generation, the time histories of p' in far field can be used to make the analysis. In order to give an in-depth view of acoustic generation, four typical virtual probes located on $\theta = 110°$, $135°$, $-135°$, and $-110°$ are selected to plotted out the time histories of p'. It should be noticed that all of these four virtual probes are located in forward half-plane. This selection is based on the calculation results shown in Section IV that the acoustic waves are mainly spreading towards forward half-plane.

Fig.19 shows the time histories of p' from t=1 to 5 at four typical virtual probes. it is apparent that the p' magnitude of FP case receives a remarkable decreasing after t=4 on all four virtual probes. This results is no surprise because Fig.18 has shown that the instability wave on suction side is weakened by the flexible panel. Since the acoustic scatter is mainly caused by the instability wave passing the trailing edge, therefore a reduction of noise generation is a quite reasonable result. A quantitative investigation on the noise reduction is also implemented by the calculation of p'_{rms}. Identical to the calculation of v'_{rms}, only a part of time history which contains five full periods is used to estimate the p'_{rms}. The time episodes are highlighted by light blue region in Fig.19 and the results of p'_{rms} are shown in Tab.4. It can be observed that for all four virtual probes, a noise reduction happens. Moreover, it is also noticeable that the noise reduction at $\theta = \pm 110°$ are much larger than the counterpart at $\theta = \pm 135°$. This implies the noise reduction is not an uniform distribution. Therefore, an azimuthal map of p'_{rms} might be needed.

$\theta(^\circ)$	p'_{rms}		
	FP1	RS1	Difference (%)
110	1.8393×10^{-4}	2.0119×10^{-4}	-8.5789
135	1.4821×10^{-4}	1.5582×10^{-4}	-4.8842
-135	1.4870×10^{-4}	1.5623×10^{-4}	-4.8198
-110	1.8849×10^{-4}	2.0482×10^{-4}	-7.9729

Table 4 p'_{rms} comparison between FP case and RS case with altered locations in far field.

Fig.20 shows a comparison of azimuthal p'_{rms} between the FP case and RS case. It is apparent that the p'_{rms} of FP case is much smaller than the one of RS case in both suction and pressure sides. This also implies the sound reduction happens in all directions. Moreover, it can be observed that the sound wave mainly propagates into two symmetrical sectors from $\theta = 30^\circ$ to 150° and $\theta = 210^\circ$ to 330°. The light gray regions in Fig.20 highlight these two regions. However, for the sectors from $\theta = 150^\circ$ to 210° and $\theta = 30^\circ$ to 330°, it can be observed that the p'_{rms} decreases to a noticeable low level, which implies there are seldom of sound wave spreading into this region. Therefore, these two regions do not play a significant role in noise reduction. Based on the azimuthal p'_{rms} map, the reduction of sound pressure level in dB might be calculated as shown in Fig.21. The definition of sound pressure level reduction ΔSPL is

$$\Delta SPL = 20 \times log_{10} \left(\frac{p'_{rms,\ FP}}{p'_{rms,\ RS}} \right) \tag{29}$$

It is found that, due to the application of flexible panel, a maximum noise reduction of 1.3dB is received which happens at $\theta = \pm 70^\circ$. For most of directions, the noise reduction is larger than 0.6dB. This strongly implies the application of flexible panel receives an appealing effect.

VI. Conclusion and remarks

The linear stability analysis is used to predict the noise generation when applying flexible panel on NACA0012 airfoil. The calculation results show that with the proper flexible panel parameters, the noise generation can be reduced up to around 1.3dB for specific direction. A spatial averaged reduction around 0.6dB is also found. These results show there might be a potential way to reduce the airfoil tonal noise with the application of flexible panel.

VII. Acknowledgments

The authors acknowledge the support given by the Central Research Grant of The Hong Kong Polytechnic University under grant no. G-YBGF. The third author gratefully acknowledges the support given by a research donation from Philip K. H. Wong Foundation under grant no. 5-ZH1X.

References

[1] Paterson, R. W., Vogt, P. G., Fink, M. R., and Munch, C. L., "Vortex noise of isolated airfoils," *Journal of Aircraft*, Vol. 10, No. 5, 1973, pp. 296–302.

[2] Tam, C. K., "Discrete tones of isolated airfoils," *The Journal of the Acoustical Society of America*, Vol. 55, No. 6, 1974, pp. 1173–1177.

[3] Longhouse, R. E., "Vortex shedding noise of low tip speed, axial flow fans," *Journal of sound and vibration*, Vol. 53, No. 1, 1977, pp. 25–46.

[4] Arbey, H., and Bataille, J., "Noise generated by airfoil profiles placed in a uniform laminar flow," *Journal of Fluid Mechanics*, Vol. 134, 1983, pp. 33–47.

[5] Brooks, T. F., and Marcolini, M. A., "Scaling of airfoil self-noise using measured flow parameters," *AIAA journal*, Vol. 23, No. 2, 1985, pp. 207–213.

[6] Nash, E. C., Lowson, M. V., and McAlpine, A., "Boundary-layer instability noise on aerofoils," *Journal of Fluid Mechanics*, Vol. 382, 1999, pp. 27–61.

[7] Desquesnes, G., Terracol, M., and Sagaut, P., "Numerical investigation of the tone noise mechanism over laminar airfoils," *Journal of Fluid Mechanics*, Vol. 591, 2007, pp. 155–182.

[8] de Pando, M. F., Schmid, P. J., and Sipp, D., "A global analysis of tonal noise in flows around aerofoils," *Journal of Fluid Mechanics*, Vol. 754, 2014, pp. 5–38.

[9] Jones, L., Sandberg, R., and Sandham, N., "Direct numerical simulations of forced and unforced separation bubbles on an airfoil at incidence," *Journal of Fluid Mechanics*, Vol. 602, 2008, pp. 175–207.

[10] Jones, L. E., and Sandberg, R. D., "Numerical analysis of tonal airfoil self-noise and acoustic feedback-loops," *Journal of Sound and Vibration*, Vol. 330, No. 25, 2011, pp. 6137–6152.

[11] Howe, M. S., "Noise produced by a sawtooth trailing edge," *The Journal of the Acoustical Society of America*, Vol. 90, No. 1, 1991, pp. 482–487.

[12] Dassen, T., Parchen, R., Bruggeman, J., and Hagg, F., "Results of a wind tunnel study on the reduction of airfoil self-noise by the application of serrated blade trailing edges," *Proc. of the European Union Wind Energy Conference and Exhibition (Göteborg, Sweden)*, 1996.

[13] Oerlemans, S., Schepers, J., Guidati, G., and Wagner, S., "Experimental demonstration of wind turbine noise reduction through optimized airfoil shape and trailing-edge serrations," 2001.

[14] Oerlemans, S., Fisher, M., Maeder, T., and Kögler, K., "Reduction of wind turbine noise using optimized airfoils and trailing-edge serrations," *AIAA journal*, Vol. 47, No. 6, 2009, pp. 1470–1481.

[15] Lam, G. C., Leung, R. C., Seid, K., and Tang, S., "Validation of CE/SE scheme in low mach number direct aeroacoustic simulation," *International Journal of Nonlinear Sciences and Numerical Simulation*, Vol. 15, No. 2, 2014, pp. 157–169.

[16] Lam, G., Leung, R., and Tang, S., "Aeroacoustics of duct junction flows merging at different angles," *Journal of Sound and Vibration*, Vol. 333, No. 18, 2014, pp. 4187–4202.

[17] Huerre, P., and Monkewitz, P. A., "Local and global instabilities in spatially developing flows," *Annual review of fluid mechanics*, Vol. 22, No. 1, 1990, pp. 473–537.

[18] Mack, L. M., "Boundary-layer linear stability theory," 1984.

[19] Drasin, P. G., and Reid, W. H., *Hydrodynamic Stability*, Cambridge university press, 2004.

[20] Theofilis, V., "Advances in global linear instability analysis of nonparallel and three-dimensional flows," *Progress in Aerospace Sciences*, Vol. 39, No. 4, 2003, pp. 249–315.

[21] Mcalpine, A., Nash, E. C., and Lowson, M. V., "On the Generation of Discrete Frequency Tones by the Flow around an Aerofoil," *Journal of Sound and Vibration*, Vol. 222, No. 5, 1999, p. 753–779.

[22] Jones, L., Sandberg, R., and Sandham, N., "Stability and receptivity characteristics of a laminar separation bubble on an aerofoil," *Journal of Fluid Mechanics*, Vol. 648, 2010, pp. 257–296.

[23] Almutairi, J. H., Jones, L. E., and Sandham, N. D., "Intermittent Bursting of a Laminar Separation Bubble on an Airfoil," *Aiaa Journal*, Vol. 48, No. 2, 2015, pp. 414–426.

[24] Tam, C. K., and Ju, H., "Aerofoil tones at moderate Reynolds number," *Journal of Fluid Mechanics*, Vol. 690, 2012, pp. 536–570.

[25] Blevins, R. D., and Plunkett, R., "Formulas for natural frequency and mode shape," *Journal of Applied Mechanics*, Vol. 47, 1980, p. 461.

[26] Fan, H. K., Leung, R. C., Lam, G. C., and Li, K., "Acoustic-structural interaction of flexible walls in a flow duct," *Proceedings of the 21th International Congress on Sound and Vibration, Beijing, China*, 2014, pp. 13–17.

[27] Fan, H. K., Leung, R. C., and Lam, G. C., "Numerical analysis of aeroacoustic-structural interaction of a flexible panel in uniform duct flow," *The Journal of the Acoustical Society of America*, Vol. 137, No. 6, 2015, pp. 3115–3126.

[28] Leung, R. C., Fan, H. K., and Lam, G. C., "A numerical methodology for resolving aeroacoustic-structural response of flexible panel," *Flinovia-Flow Induced Noise and Vibration Issues and Aspects*, Springer, 2015, pp. 321–342.

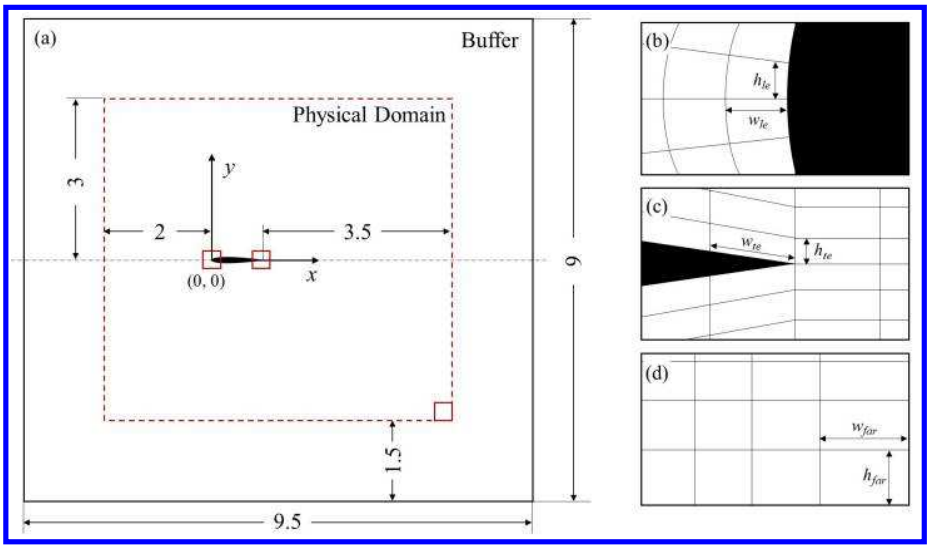

Fig. 1 Schematic sketch of physical (red) and computational domain.

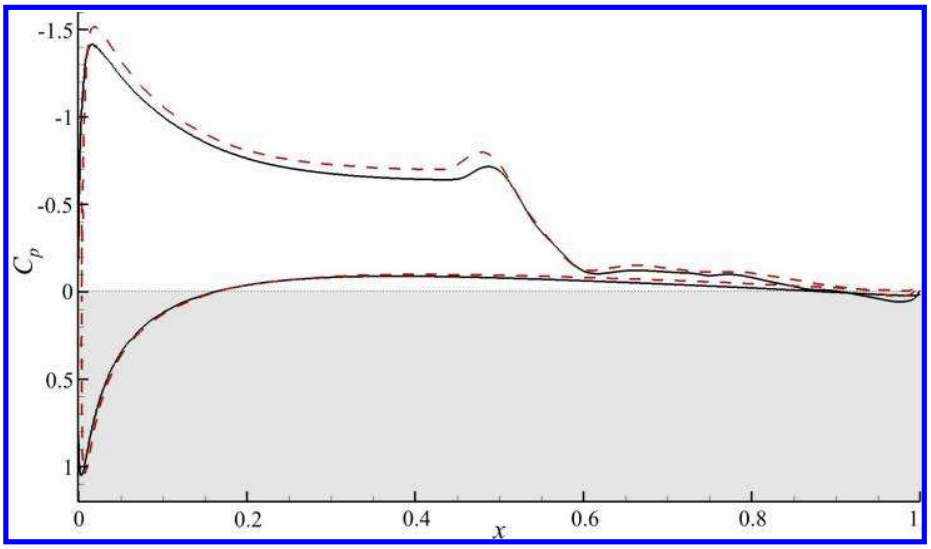

Fig. 2 Distribution of C_p on airfoil. ——, CE/SE result, - - -, result of Jones (et al).

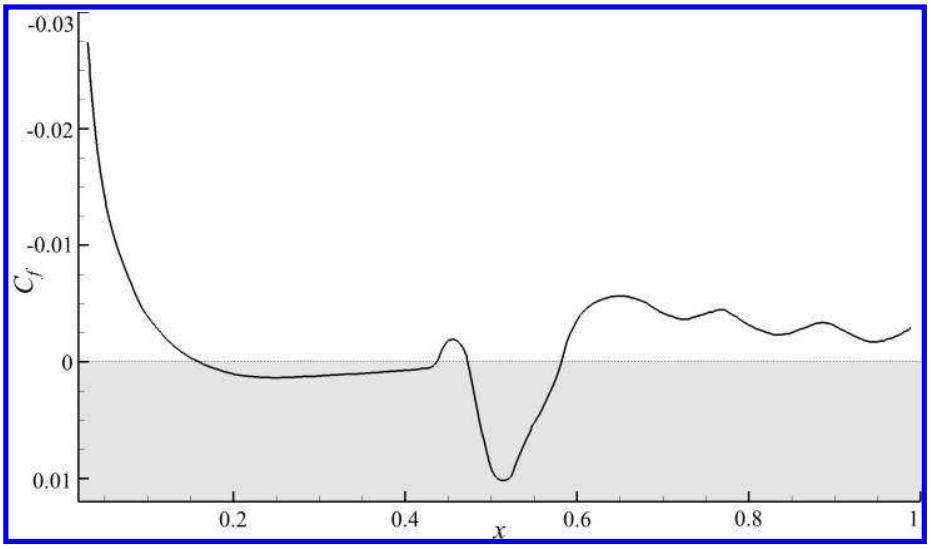

Fig. 3 Distribution of C_f.

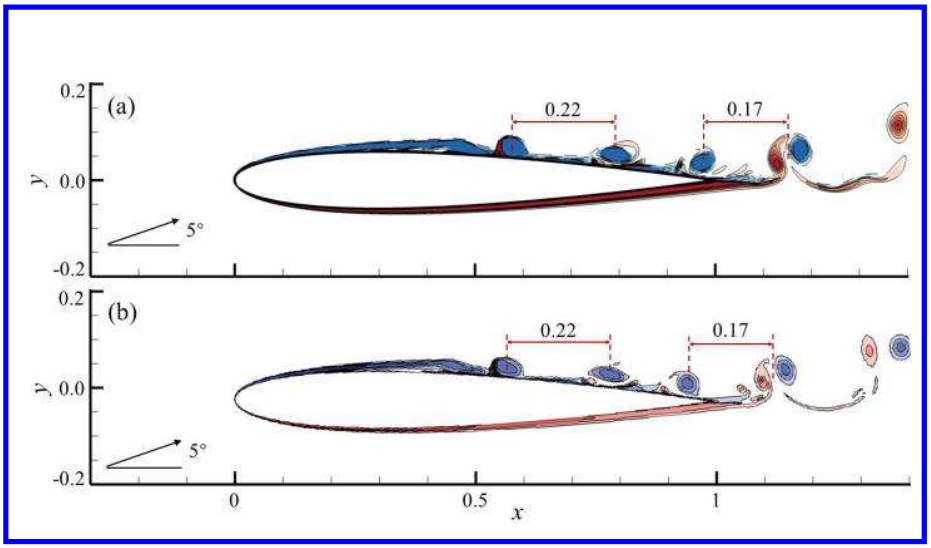

Fig. 4 Iso-contours of vorticity by (a), CE/SE and (b), result of Jones (et al).

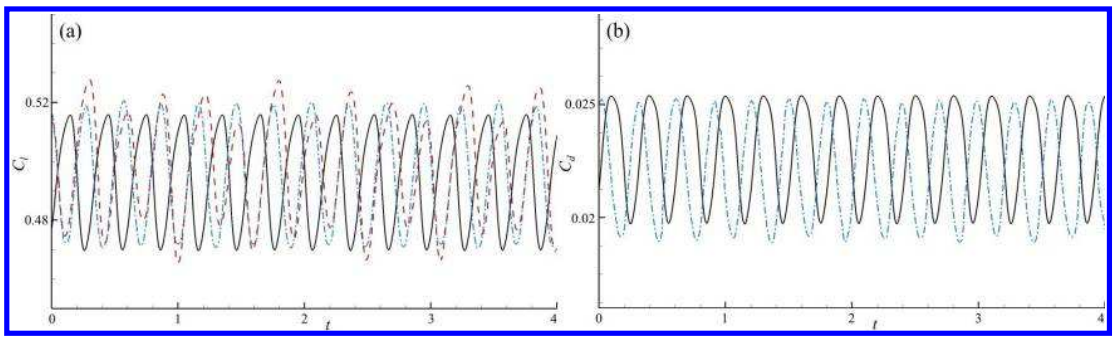

Fig. 5 Comparisons of (a) C_l and (b) C_d. ——, CE/SE result, - - -, result of Jones (et al), -·-·-, result of Almutairi (et al)

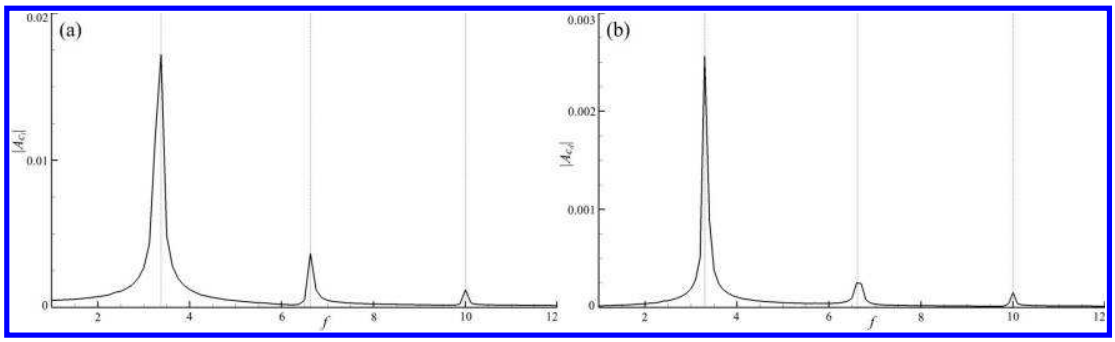

Fig. 6 Spectra of (a) C_l and (b) C_d.

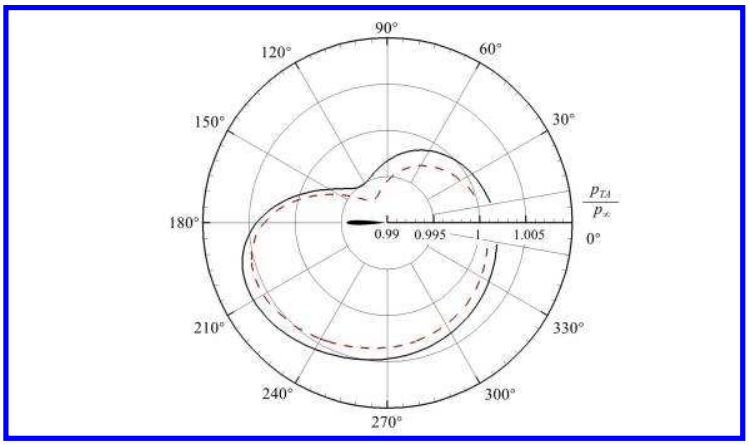

Fig. 7 Comparison of $\bar{p}/p_\infty$ at radius two. ——, CE/SE result; - - -, result of Jones (et al).

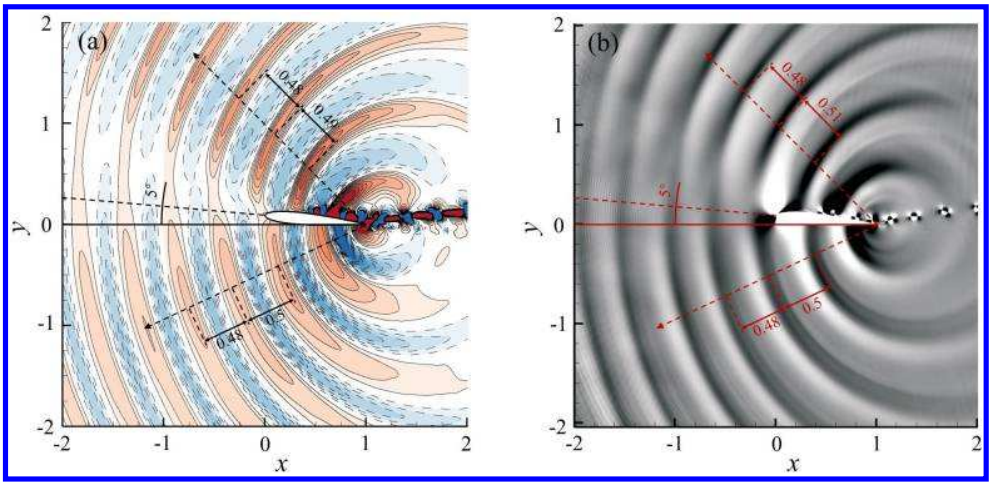

Fig. 8 Comparison of instantaneous acoustic field. (a), CE/SE result; (b), result of Jones (et al).

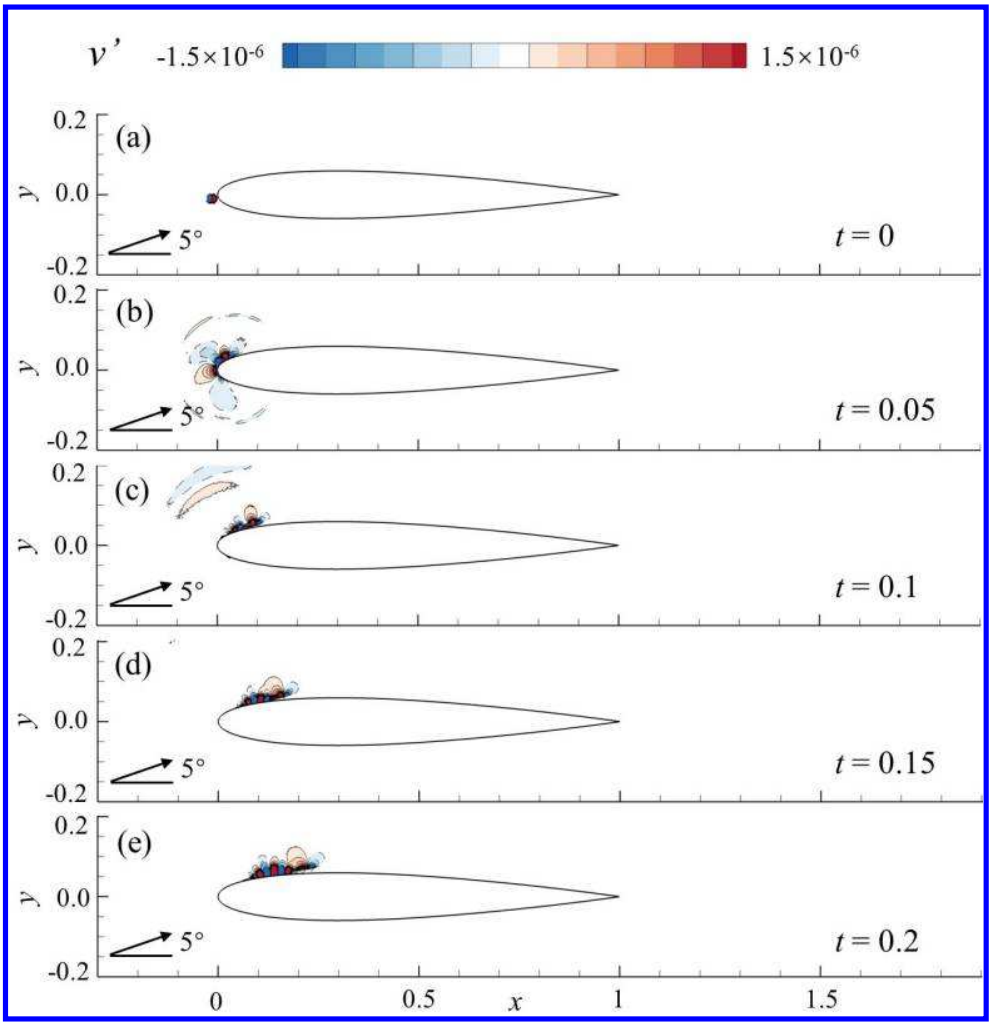

Fig. 9 Iso-contour of v' from t=0.0 to 0.2 with interval 0.05. The negative contours represented as the dashed lines.

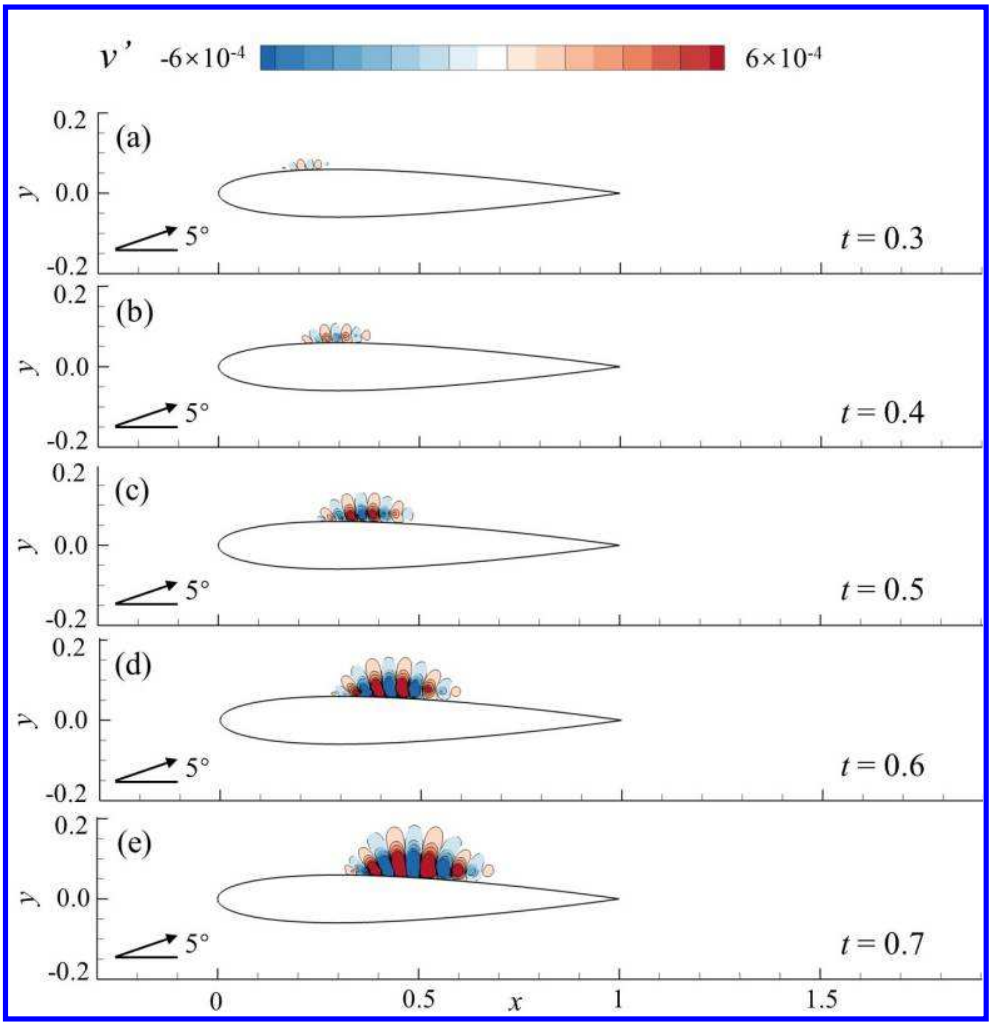

Fig. 10 Iso-contour of v' from t=0.3 to 0.7 with interval 0.1. The negative contours represented as the dashed lines.

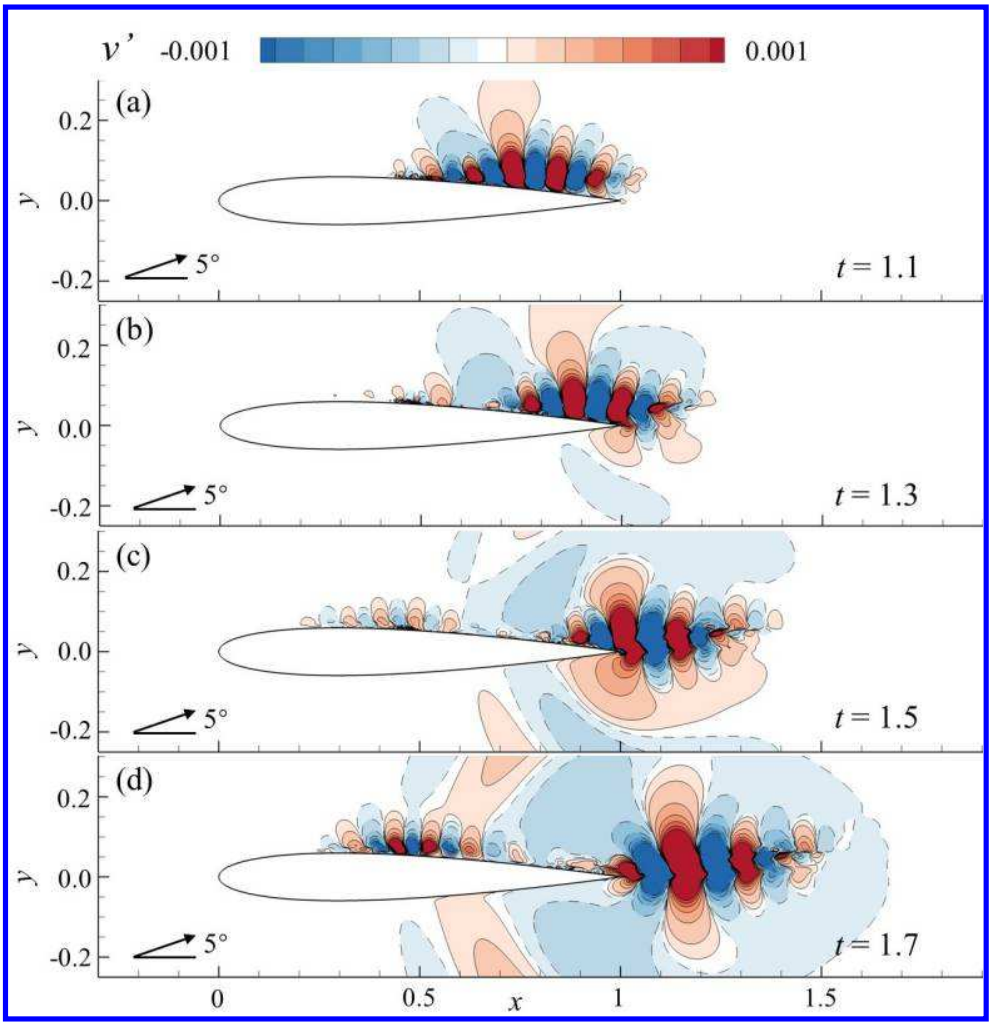

Fig. 11 Iso-contour of v' from t=1.1 to 1.7 with interval 0.2. The negative contours represented as the dashed lines.

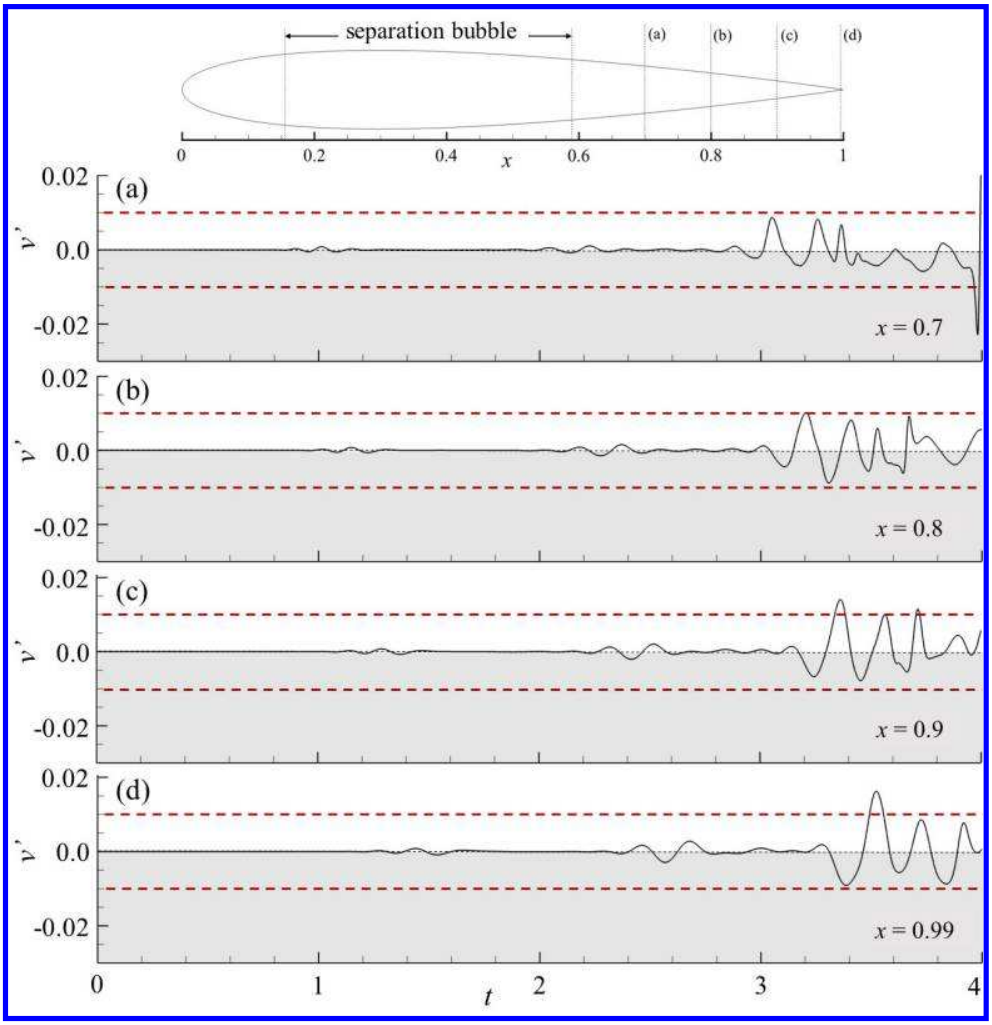

Fig. 12 Time histories of v' at four altered locations.

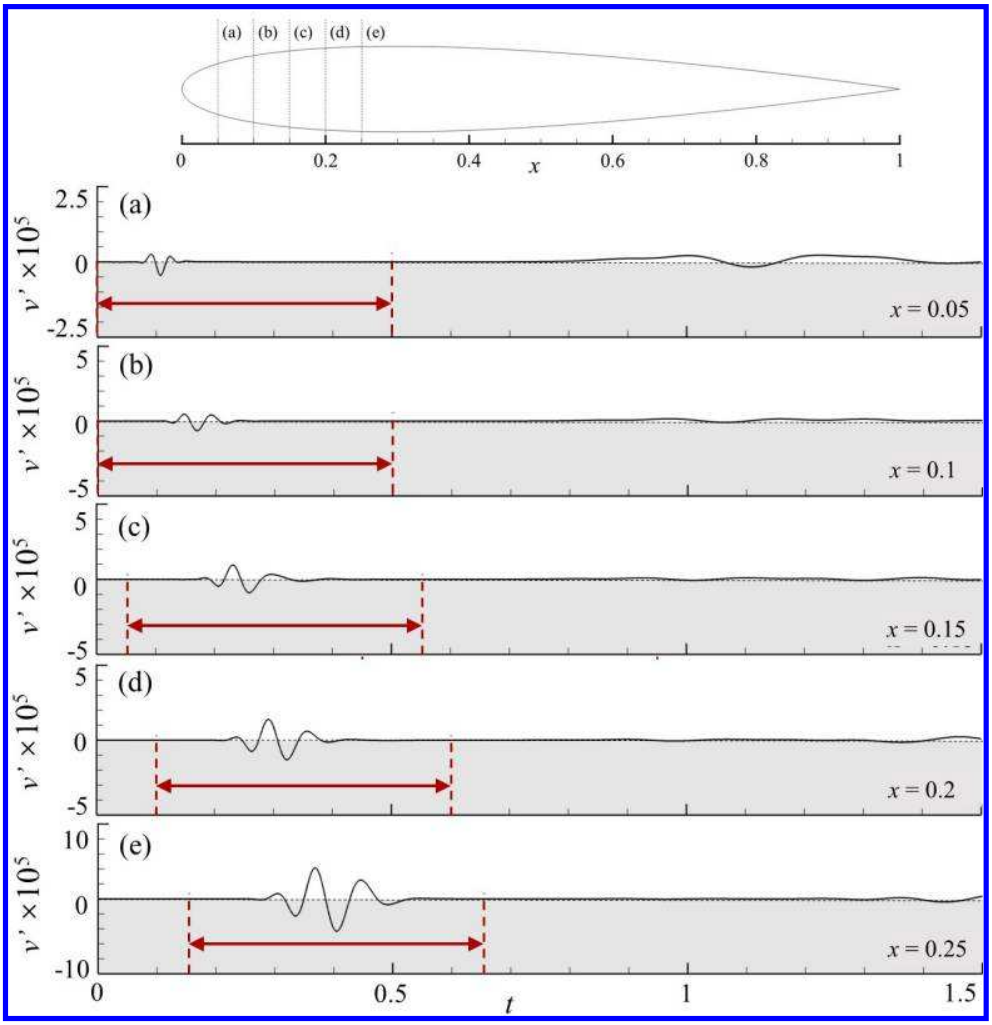

Fig. 13 For caption see next page

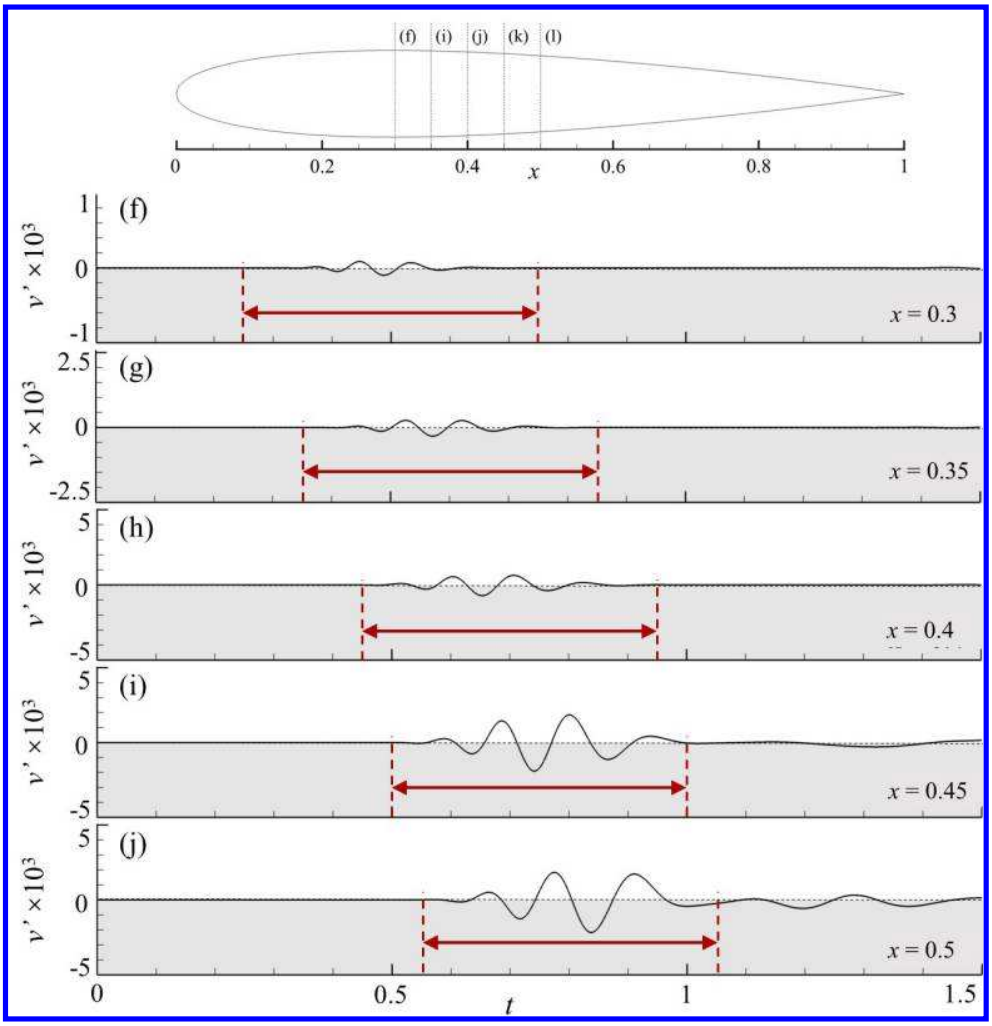

Fig. 14 The v' time histories on altered locations. (a), x=0.05, (b), x=0.1, (c), x=0.15, (d), x=0.2, (e), x=0.25, (f), x=0.3, (g), x=0.35, (h), x=0.4, (i), x=0.45, (i), x=0.5.

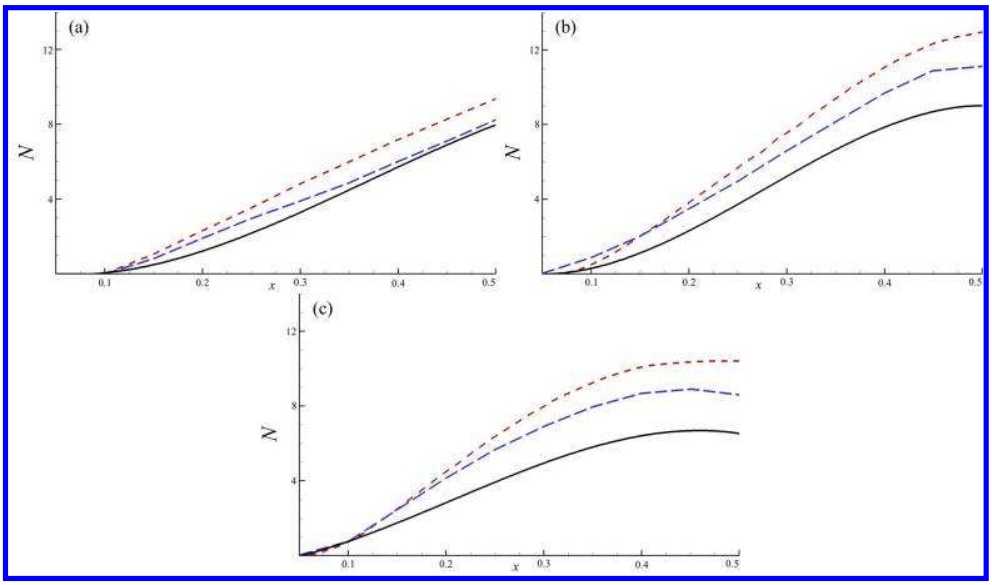

Fig. 15 Comparison of N-factor among altered frequencies. (a), f=4.24, (b), f=8.49, (c), f=12.37. ——, 2D CE/SE result, - - -, 2D O-S Equation result by Jones (et al). — —, 3D result of Jones (et al).

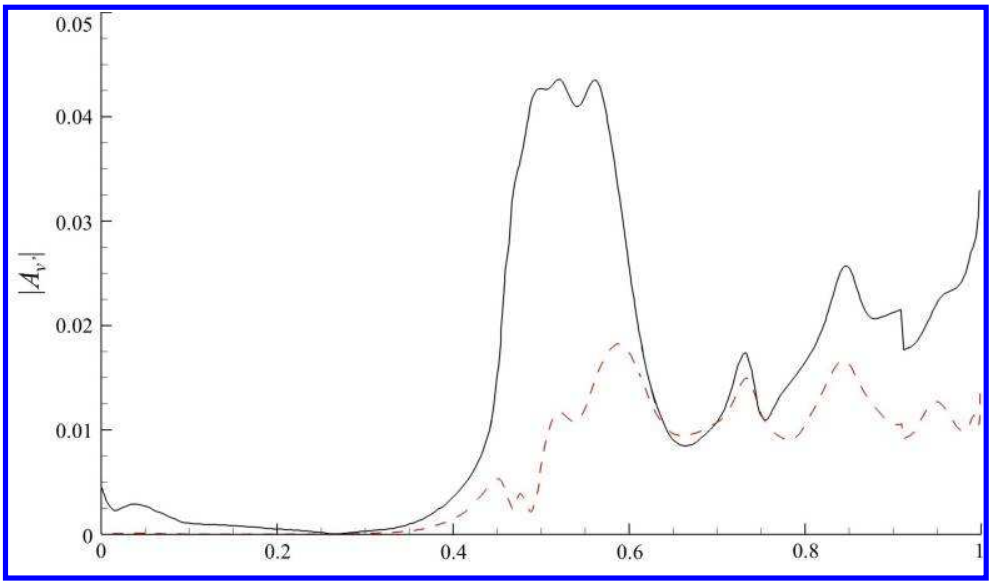

Fig. 16 Amplitude variation of v' along chordwise. ——, $f_{flow,1}$=3.3, - - -, $f_{flow,2}$=6.7.

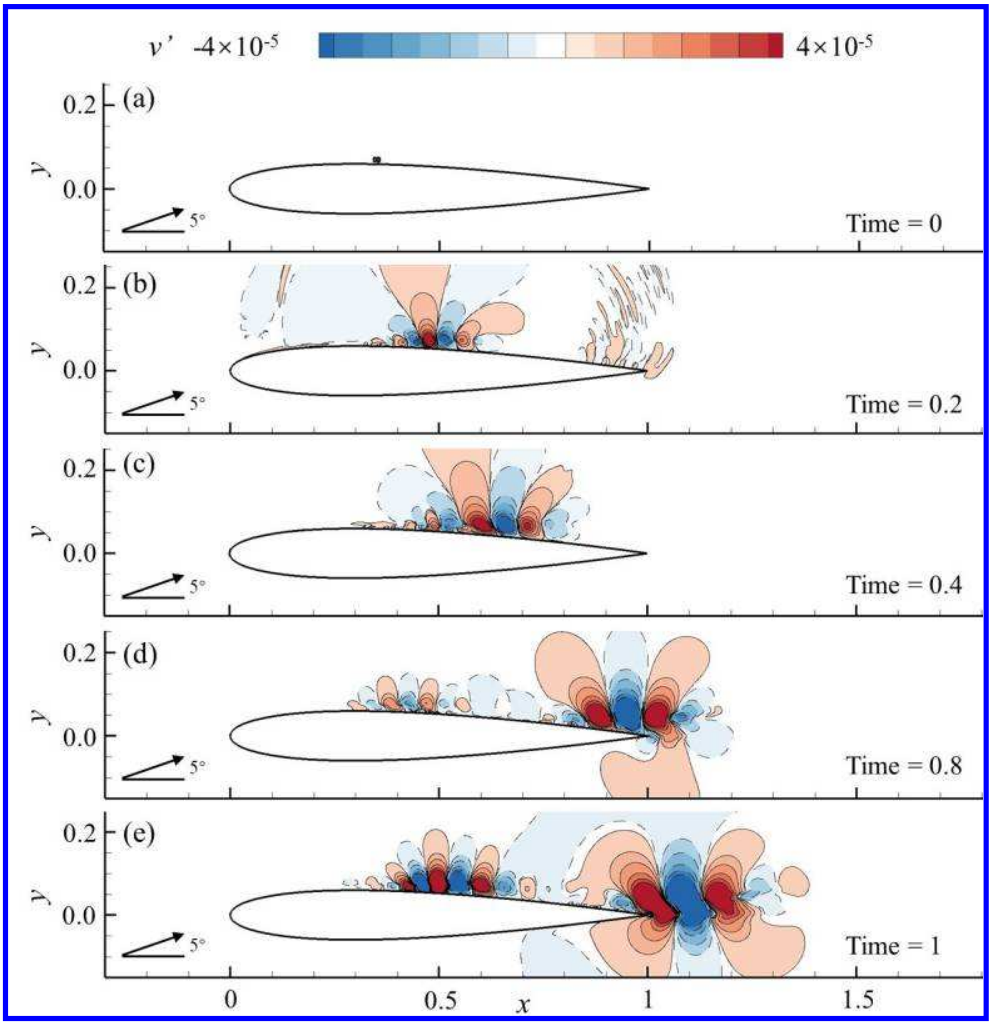

Fig. 17 Iso-contour of v' in FP case from t=0 to 1. The negative contours represented as the dashed lines.

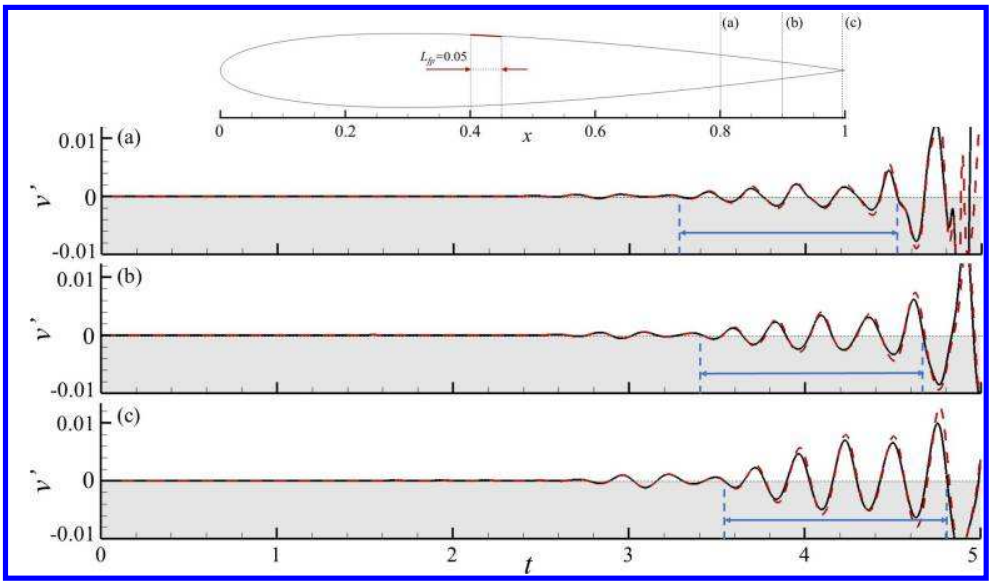

Fig. 18 The comparison of v' time histories between FP case and RS case at locations x=0.8, 0.9 and 0.99. ——, FP case, - - -, RS case.

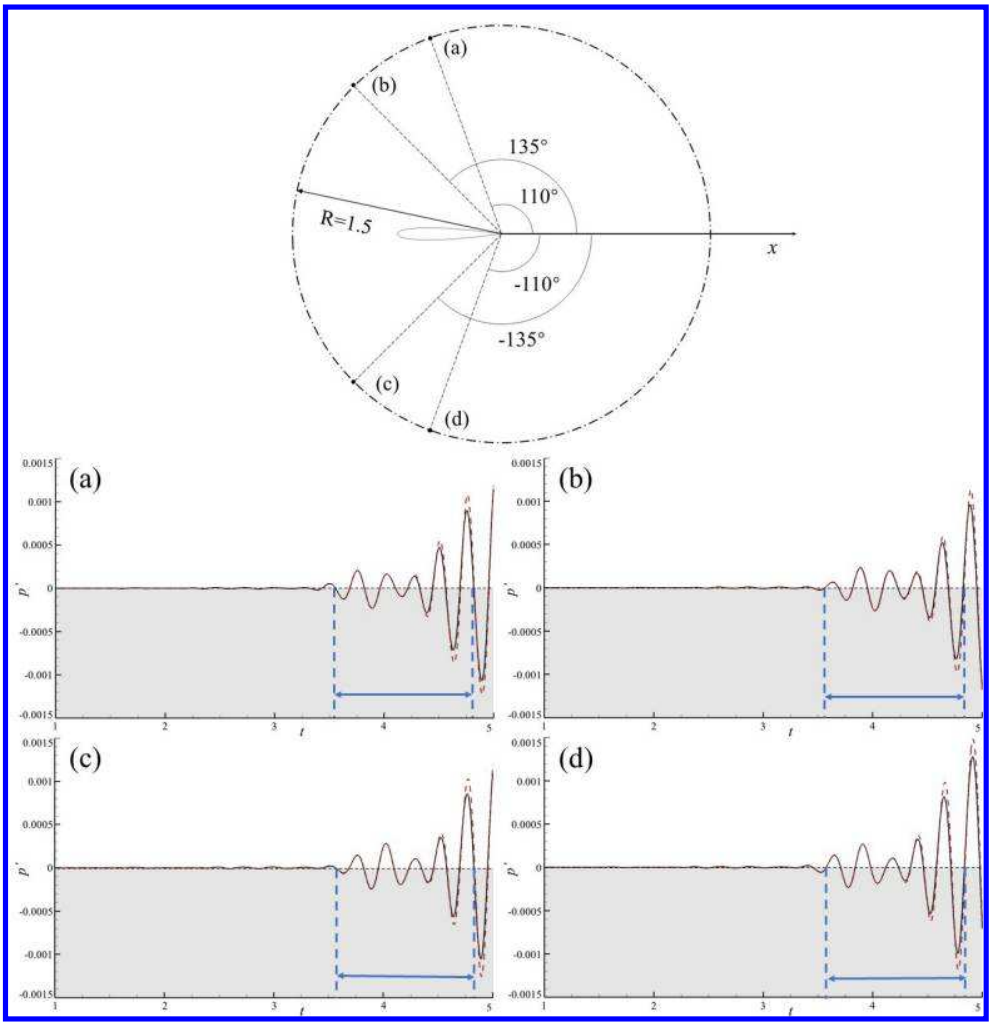

Fig. 19 Comparison of p' time histories between FP case and RS case at four typical virtual probes. ——, FP case, - - -, RS case.

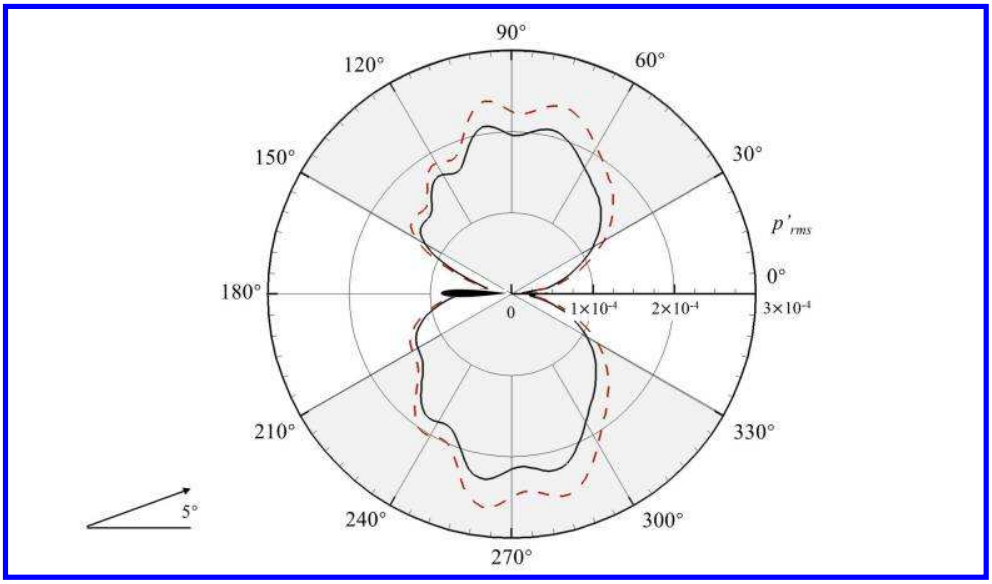

Fig. 20 Azimuthal p'_{rms} comparison between FP case and RS case. ——, FP case, - - -, RS case.

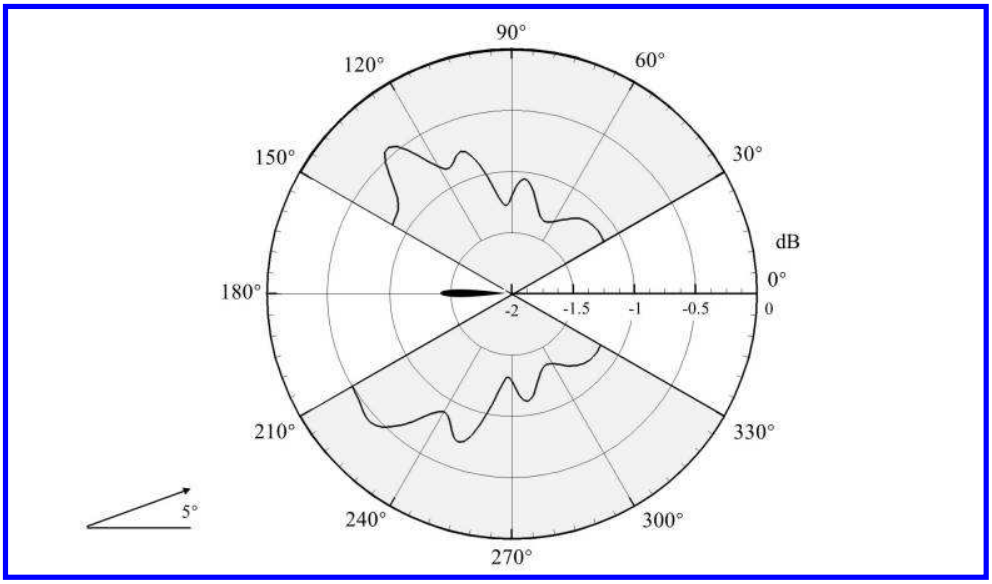

Fig. 21 Azimuthal noise reduction map.